Supporting Information

Insight into the $CH_3NH_3PbI_3$/C interface in hole-conductor-free mesoscopic perovskite solar cells

Jiangwei Li,[a] Guangda Niu,[a] Wenzhe Li,[a] Kun Cao,[b] Mingkui Wang[b] and Liduo Wang[a]*

a Department of Chemistry, Tsinghua University, Beijing 100084, P. R. China. E-mail: chldwang@mail.tsinghua.edu.cn
b Wuhan National Laboratory for Optoelectronics, Huazhong University of Science and Technology, Wuhan 430074, P.R. China

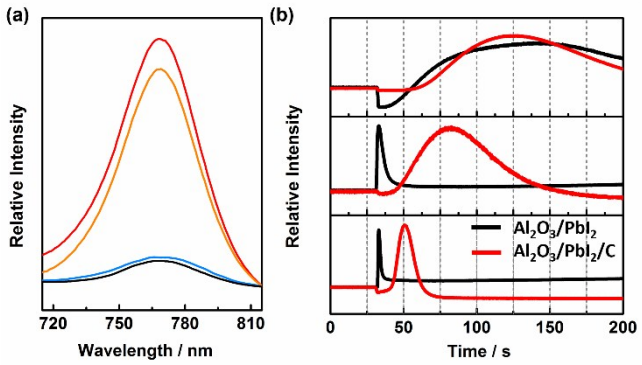

Figure S1. (a) Steady-state PL spectra of $Al_2O_3/CH_3NH_3PbI_3$ before (orange) and after (red) annealing excited from the perovskite film side, $Al_2O_3/CH_3NH_3PbI_3$ (blue) and $Al_2O_3/C/CH_3NH_3PbI_3$ (black) without annealing excited from the glass side. Note that the maximum intensity locate at around 768 nm for all case. (b) Time evolution of the PL intensity of $CH_3NH_3PbI_3$ during reaction of PbI_2 with different concentration of CH_3NH_3I solution (from top to bottom: 0.032 M, 0.063 M and 0.126 M).

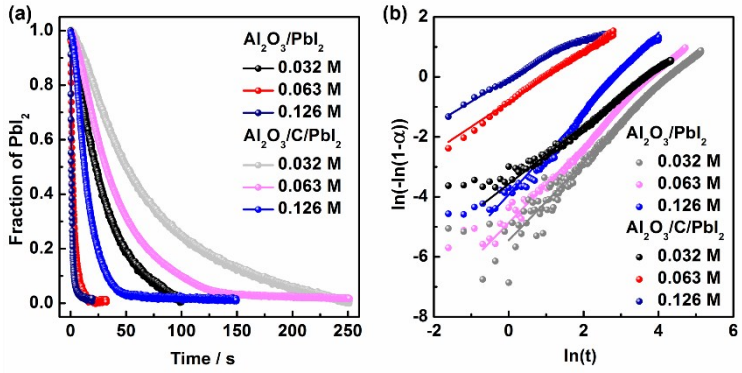

Figure S2. (a) The fraction of PbI_2 derived from PL intensity decay. (b) The Avrami model fit for the "two-step" reaction with different concentration of CH_3NH_3I solution and substrates and the Avrami model parameters are shown in **Table S1**.

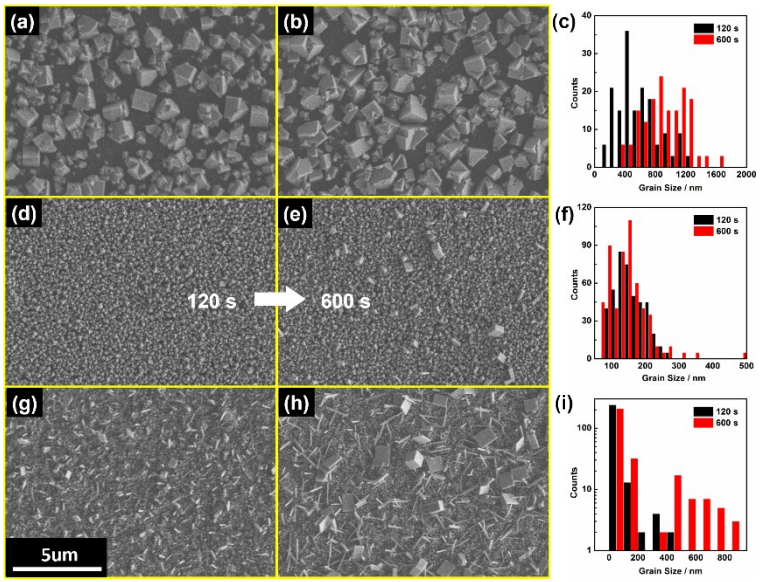

Figure S3. SEM images of $Al_2O_3/CH_3NH_3PbI_3$ obtained by different concentration of CH_3NH_3I solution (0.032 M for (a), (b); 0.063 M for (d), (e); 0.126 M for (g), (h)) with different dipping time (120 s for (a), (d), (g) and 600 s for (b), (e), (h)). The crystal size distribution for each case is presented in (c), (f) and (i).

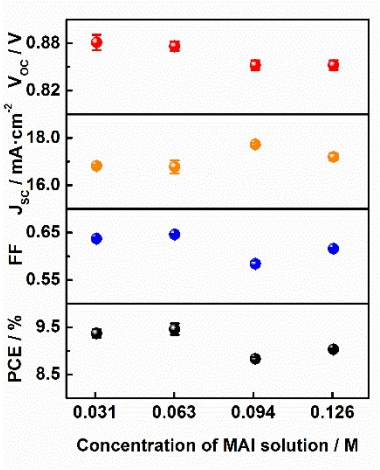

Figure S4. Solar cell performance of the carbon-electrode mesoscopic PSCs with different concentration of CH_3NH_3I solution in the "two-step" preparation process. The neglectable effect of CH_3NH_3I solution concentration on the photovoltaic performance, compared with normal devices with spiro-MeOTAD hole transport layer and gold electrode, indicated a similar $CH_3NH_3PbI_3$/C interfacial condition by the carbon layer confinement.[1]

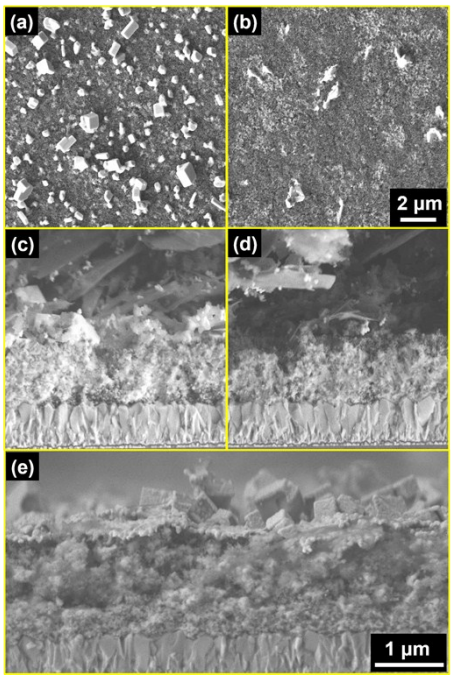

Figure S5. SEM images of the $TiO_2/Al_2O_3/CH_3NH_3PbI_3$ substrate (a) before and (b) after DMF vapor treatment ($CH_3NH_3PbI_3$-DVT). Cross-sectional SEM images of

$TiO_2/Al_2O_3/C/CH_3NH_3PbI_3$ substrate (a) before and (b) after DMF vapor treatment ($CH_3NH_3PbI_3$-DVT) and (e) the $TiO_2/Al_2O_3/CH_3NH_3PbI_3$/Au device.

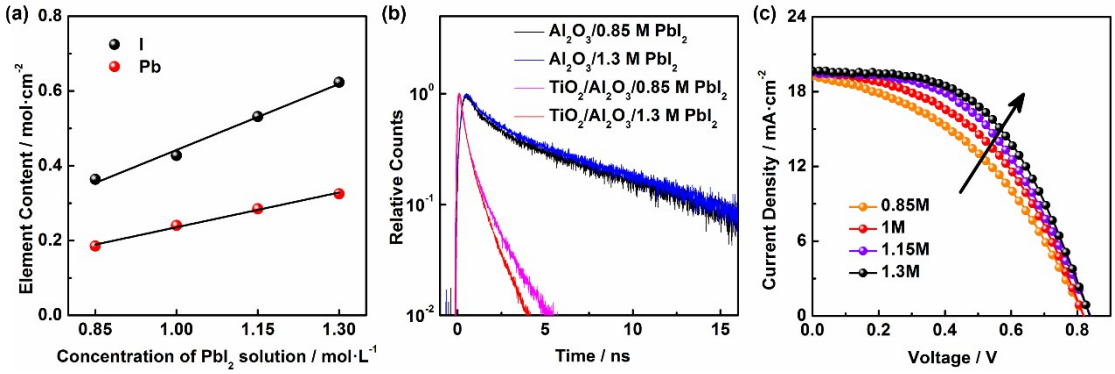

Figure S6. (a) Pb and I element content of the spin-coating prepared $TiO_2/Al_2O_3/PbI_2$ film determined by ICP-AES for different PbI_2 concentration, which demonstrated a linear change of PbI_2 filling in the mesoporous substrates. (b) Time-resolved PL decay of $CH_3NH_3PbI_3$ film obtained by different concentration of PbI_2 on different substrate (Al_2O_3 scaffold for the intrinsic PL lifetime and TiO_2 for electron quenching process). The fitted PL lifetime of both intrinsic and electron quenched $CH_3NH_3PbI_3$ were in good agreement with previous reports.[2] The steady-state PL spectra are in **Figure S8**a. (c) J-V curves of the carbon-electrode mesoscopic PSCs with different concentration of PbI_2 solution. As the concentration of PbI_2 solution increased, better light harvest and more efficient electron extraction are achieved by larger amount of $CH_3NH_3PbI_3$ and their more sufficient contact with the TiO_2 photoanode, respectively, leading to the increase of FF.

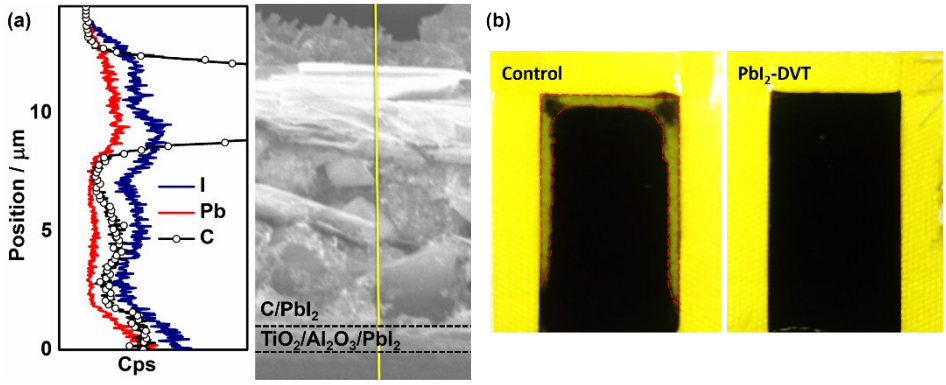

Figure S7. (a) Cross-sectional SEM image and EDS line scanning (yellow line) of $TiO_2/Al_2O_3/C/PbI_2$. (b) Photographs of the carbon-electrode mesoscopic PSCs with (right) and without (left) PbI_2-DVT method. The red dash line in the control group photograph outlines the visible unreacted PbI_2 area.

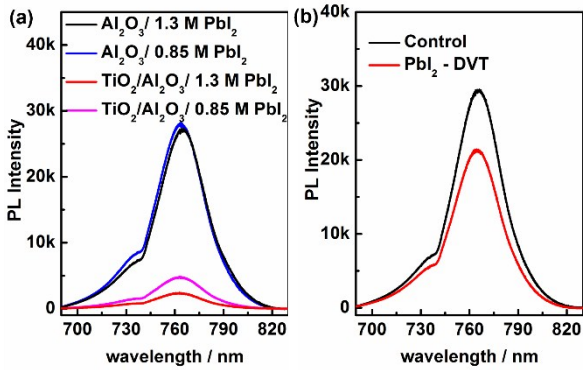

Figure S8. (a) Electron extraction induced steady-state PL quenching for different concentration of PbI_2 solution. (b) Steady-state PL spectra of $Al_2O_3/C/CH_3NH_3PbI_3$ film with and without PbI_2-DVT method. Note that this part of PL results were acquired by HORIBA Evolution with excitation of 514 nm laser and the abnormal hump of the curves before 740 nm is attributed to the instrumental error during switching received PL emission wavelength range of the detector.

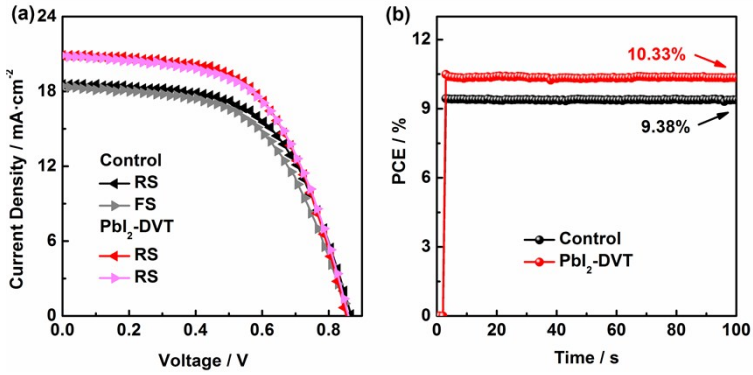

Figure S9. (a) The hysteresis characteristics and (b) The maximum power point of tracking for devices in **Figure 6**a.

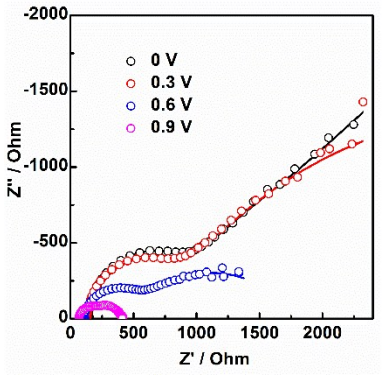

Figure S10. Nyquist Plots of EIS measurements under illumination and a bias at 0, 0.3, 0.6 and 0.9 V for the carbon-electrode mesoscopic PSCs. The solid lines are the fitting results. There are two typically R-C circuit components in the high and medium frequency regions, respectively, and the discrete feature in the low frequency is not shown. The R_{CE} was extracted as the fitted high frequency resistance value.[3]

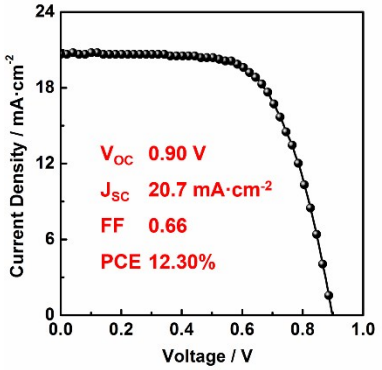

Figure S11. The champion device of the carbon-electrode mesoscopic PSCs with PbI_2-DVT. Inset shows the corresponding photovoltaic parameter.

Table S1. Estimated reaction rate constants (k) and exponents (n) for the "two-step" reaction with different concentration of CH_3NH_3I solution and substrates.

Concentration of CH_3NH_3I solution [M]	Substrates	1000k [s^{-1}]	n	Substrates	1000k [s^{-1}]	n
0.032	Al_2O_3/PbI_2	28.2 ±0.3	0.967	$Al_2O_3/C/PbI_2$	4.30 ±0.07	1.29
0.063	Al_2O_3/PbI_2	436 ±4	0.828	$Al_2O_3/C/PbI_2$	7.71 ±0.08	1..28
0.126	Al_2O_3/PbI_2	936 ±6	0.754	$Al_2O_3/C/PbI_2$	39.7 ±0.7	1.35

Table S2. Summary of the parameters using biexponential decay fit for the Time-resolved PL decay curves showed in **Figure S6**b.

Meso	c[PbI_2] [$mol \cdot L^{-1}$]	<τ> [ns]	A1	τ1 [ns]	A2	τ2 [ns]
Al_2O_3	0.85	6.80 ±0.51	0.49	12.6 ±0.2	0.51	1.22 ±0.04
Al_2O_3	1.3	8.22 ±0.47	0.53	14.3 ±1.1	0.47	1.27 ±0.06
TiO_2	0.85	0.620 ±0.002	0.19	1.65 ±0.01	0.81	0.380 ±0.002
TiO_2	1.3	0.501 ±0.002	0.23	1.15 ±0.01	0.77	0.303 ±0.004

Avrami model for reaction kinetics

The perovskite reaction kinetics with different concentration and different substrates was acquired with the generalized Avrami model.[4] This kinetic model is normally used to describe solids transformation from one phase to another under isothermal condition as follow,

$$\alpha(t) = 1 - \exp(-kt^n) \quad (1)$$

$$\ln[-\ln(1-\alpha(t))] = \ln k + n \ln t \quad (2)$$

where α(t) is the fraction of reacted PbI_2 derived from PL intensity ($1-I_t/I_{initial}$) at time t from the induction time and k is the crystal growth rate constant. Note that the baseline at t=∞ is deducted for I_t for accuracy. The fraction of PbI_2 is shown in **Figure S2**a and fitted with **Equation 2** to obtain the reaction rate constant (k) and the Avrami exponent (n), summarized

in **Table S2**. The extracted value n provided information of the crystallization mechanism, since the Avrami approach was deduced from the balance between nucleation and crystal growth. The original derivation of the Avrami exponent was for three limiting cases, where n=0~2 was for one-dimensional growth, n=2~3 for two-dimensional growth and n=3~4 for three-dimensional growth.[5] For a typical case of n between 0.5 to 1.5, which was based on a modified model by Hulbert, the phase transformation was considered to be an one-dimensional and diffusion-controlled reaction. If the nucleation is instantaneous, n would be close to 0.5; if the nucleation rate is constant, n would be close to 1.5.[6] Clearly, in our cases, the values of n in the range of 0.5~1.5 indicated an one-dimensional and diffusion-controlled growth mechanism. The transformation from PbI_2 to $CH_3NH_3PbI_3$ phase and the consequential crystallization process was confined by the mesoporous Al_2O_3 and TiO_2 templates and controlled by the infiltration of CH_3NH_3I solution. In addition, the values of n for the Al_2O_3/PbI_2 substrates were more close to 0.5 while for the $Al_2O_3/C/PbI_2$ substrates, they were more close to 1.5, inferring an instantaneous nucleation mechanism through direct contact of CH_3NH_3I reagent and a constant nucleation rate by the confinement effect of the carbon layer, respectively.

1. Schlipf, J.; Docampo, P.; Schaffer, C. J.; Körstgens, V.; Bießmann, L.; Hanusch, F.; Giesbrecht, N.; Bernstorff, S.; Bein, T.; Müller-Buschbaum, P. *J. Phys. Chem. Lett.* 2015, *6*, 1265; b) Im, J.; Jang, I.; Pellet, N.; Grätzel, M.; Park, N. *Nat. Nanotechnol.* 2014, *9*, 927.
2. Mei, A.; Li, X.; Liu, L.; Ku, Z.; Liu, T.; Rong, Y.; Xu, M.; Hu, M.; Chen, J.; Yang, Y.; Gratzel, M.; Han, H. *Science* 2014, *345*, 295.
3. Xu, X.; Liu, Z.; Zuo, Z.; Zhang, M.; Zhao, Z.; Shen, Y.; Zhou, H.; Chen, Q.; Yang, Y.; Wang, M. *Nano Lett.* 2015, *15*, 2402.
4. Avrami, M. *J. Chem. Phys.* 1941, 9, 177.
5. Kim, W. K.; Payzant, E. A.; Yoon, S.; Anderson, T. J. *J. Cryst. Growth.* 2006, 294, 231.

6. J. D. Hancock, J. H. Sharp, *J. Am. Ceram. Soc.* 1972, 55, 74.